JGR Oceans

RESEARCH ARTICLE
10.1029/2022JC018437

Surface Wave and Roller Dissipation Observed With Shore-Based Doppler Marine Radar

Michael Streßer[1], Jochen Horstmann[1], and Burkard Baschek[1,2]

[1]Helmholtz-Zentrum Hereon, Geesthacht, Germany, [2]Now at: Deutsches Meeresmuseum, Stralsund, Germany

Key Points:

- high-resolution observations of surface wave and roller dissipation as well as the transformation of wave height across the surf zone
- the concept of surface rollers is applied to shore-based X-band Doppler radar data
- in storm conditions, 50% of the wave energy is dissipated at a submerged outer sandbar, but strongest dissipation occurs further inshore

Correspondence to:
M. Streßer,
michael.stresser@hereon.de

Citation:
Streßer, M., Horstmann, J., & Baschek, B. (2022). Surface wave and roller dissipation observed with shore-based Doppler marine radar. *Journal of Geophysical Research: Oceans*, *127*, e2022JC018437. https://doi.org/10.1029/2022JC018437

Received 14 JAN 2022
Accepted 15 AUG 2022

Author Contributions:

Conceptualization: Michael Streßer, Jochen Horstmann, Burkard Baschek
Data curation: Michael Streßer
Methodology: Michael Streßer
Software: Michael Streßer
Supervision: Jochen Horstmann, Burkard Baschek
Visualization: Michael Streßer
Writing – original draft: Michael Streßer
Writing – review & editing: Jochen Horstmann, Burkard Baschek

Abstract Surface wave energy and dissipation are observed across the surf zone. Utilizing the concept of surface rollers, a new scaling is introduced to obtain the energy flux and dissipation related to rollers from Doppler velocities measured by a shore-based X-band marine radar. The dissipation of wave energy and hence the transformation of the incoming wave height (or energy) is derived using the coupled wave and roller energy balance equations. Results are compared to in-situ wave measurements obtained from a wave rider buoy and two bottom mounted pressure wave gauges. A good performance in reproducing the significant wave height is found yielding an overall root-mean-square error of 0.22 m and a bias of −0.12 m. This is comparable to the skill of numerical wave models. In contrast to wave models, however, the radar observations of the wave and roller energy flux and dissipation neither require knowledge of the bathymetry nor the incident wave height. Along a 1.5 km long cross-shore transect on a double-barred, sandy beach in the southern North Sea, the highest dissipation rates are observed at the inner bar over a relatively short distance of less than 100 m. During the peak of a medium-severe storm event with significant wave heights over 3 m, about 50% of the incident wave energy flux is dissipated at the outer bar.

Plain Language Summary Ocean waves are carrying a large amount of mechanical energy which they have gained from the wind blowing over the ocean surface. At the coast this energy supply generates strong water motions, creates forces on coastal structures, moves sand, and can cause coastal erosion. It is therefore important to know when, where, and to what extent wave energy is reduced under different environmental conditions. The majority of the energy is removed by wave breaking. However, this process is still not completely understood which is partly due to fact that it is difficult to observe. This is particularly the case during storm conditions when it is very complicated to install and recover measurement equipment in the ocean. The present work describes a methodology to obtain such measurements using a special radar device which is installed at the beach; hence, it is not being impacted by harsh wave conditions. This approach will enable scientists to perform long-term monitoring of wave breaking thus opening new opportunities to study beach processes and coastal changes.

1. Introduction

The Earth's coastlines are facing sea level rise and increased human interventions. Predicting long-term coastal changes is of major importance to ensure efficient planning and design of coastal structures, as well as sustainable management of the coastal zone. Furthermore, a proper incorporation of nearshore processes into earth system models is required to efficiently predict the future changes of the coastal morphology, that is, coastal morphodynamics. Long-term measurements of nearshore hydrodynamics, in particular the spatial distribution of wave heights, are rarely available but often required to develop, validate, or calibrate parameterizations of nearshore processes.

Breaking surface waves are important drivers of nearshore hydro- and morphodynamics. When a wave breaks, its height and thus the energy that is contained in the wave motion at the scale of the breaker decreases. The vast majority of the extracted wave energy is irreversibly converted (dissipated) to currents (slowly varying mean flow, e.g., Longuet-Higgins & Stewart, 1964), vorticity (Clark et al., 2012), turbulence (chaotic oscillations at higher frequencies, e.g., Feddersen & Trowbridge, 2005), heat (e.g., Sinnett & Feddersen, 2014), sea spray (Van Eijk et al., 2011), sound and air entrainment (Deane, 1997), and re-suspension of sediments (Voulgaris & Collins, 2000). Therefore, wave breaking and the associated wave energy dissipation link the wave energy flux to mixing and sediment transport. A "direct measurement of wave dissipation is equivalent to measuring the forcing for nearshore flow" (Holman & Haller, 2013). However, deployment and maintenance of in-situ sensors (e.g.,

wave staffs, acoustic sensors or pressure transducers) is difficult, in particular within energetic breaking wave conditions. Moreover, a large number of instruments is required to capture the typically high spatial variability of the nearshore wave field.

This has motivated the development of close-range remote sensing techniques that are typically less accurate than in-situ sensors, but come with the major benefit of providing continuous data at high resolution in space and time. Coastal video monitoring systems are probably the most widely used sensor type. Such systems provide reasonable ground coverage and can be used to derive local bathymetry (Holman et al., 2013), currents (Chickadel et al., 2003), or both in combination (Dugan et al., 2001) from wave propagation. Visible light video techniques require daylight as a source of radiation. Thermal cameras, by contrast, also facilitate nighttime operations, although the signature physics differ between day and night (e.g., Holman & Haller, 2013). Imaging marine radar is an active remote sensing technique. As such, it can also be operated during day and night as well as in bad (foggy) view conditions. Compared to cameras, radar has typically a coarser spatial resolution but provides much larger spatial coverage and easier geo-referencing. Incoherent marine radar can be used to infer currents (Senet et al., 2001; Lund et al., 2018, among others) and bathymetry (Senet et al., 2008; Bell & Osler, 2011; Lund et al., 2018; Chernyshov et al., 2020, among others) as well as directional wave spectra (Nieto Borge et al., 1999). Radar-based retrieval of currents from wave dispersion outside the surf zone has been shown to be highly accurate, with a root-mean-square error (RMSE) below 0.04 m/s. However, in regions of enhanced wave breaking, radar and video techniques based on linear wave dispersion fail due to increasingly nonlinear wave propagation, and the change of imaging mechanisms in the presence of foam and spray. Despite their negative influence on wave dispersion based techniques, the signatures of residual foam in videos can be exploited to estimate surface current fields in the surf zone (Anderson et al., 2021; Rodríguez-Padilla et al., 2021). The retrieval of surface elevation maps from camera or radar images is more difficult because a careful interpretation of the measured signal is required to reconstruct the free surface. The use of stereo photogrammetry (Bergamasco et al., 2017; de Vries et al., 2011) for this purpose is promising, but applications and validations in the nearshore are still limited. On the contrary, scanning lidar can provide direct and highly accurate space-time measurements of the surface elevation (Carini et al., 2021a; Martins et al., 2016; O'Dea et al., 2021, among others). Lidar requires specular reflection from the surface and thus either low incidence angles, or the presence of foam, water droplets, or enough small scale roughness at the surface. Therefore, only limited distances (around 100 m) can be covered which prevents applications over wide surf zones if no infrastructure, like a pier, is available. Radar-based methods to derive wave energy could therefore help to overcome the limitations regarding the spatial coverage.

McGregor et al. (1998) estimated local wave energy and water depths before and after a sandbar through a direct inversion of the Doppler velocity observed with imaging (S-band) Doppler radar. In their study, radial velocity spectra obtained from the Doppler velocity were directly transformed to sea surface elevation spectra through linear wave theory (as described in Plant et al., 1983). Their radar system, however, was located on a cliff 80 m above the water surface; thus, grazing angles were still relatively high (between 9° and 5°). At lower grazing angles (<5°), backscatter modulation mechanisms are different and nonlinear imaging mechanisms, for example, shadowing, small-scale wave breaking, or wedge scattering, become important (for details refer to the special issue by Brown, 1998). This hinders a direct inversion of the radar signal to surface elevation. For incoherent radars, the nonlinearities resulting from the imaging are traditionally eliminated through the application of a bandpass filter around the linear wave dispersion relation in the wavenumber-frequency domain in combination with an empirical modulation transfer function (MTF, Nieto Borge et al., 1999; NietoBorge et al., 2004). This requires intensive calibration for every individual radar installation. In the nearshore, however, waves, currents, and the bathymetry vary on short distances. Therefore, the homogeneity assumption is violated and it is often not possible to apply a properly defined dispersion filter. In homogeneous conditions, a calibration-free measurement of the significant waves height is possible using Doppler radar (Carrasco et al., 2017), but the need for dispersion filtering remains. Recently, Navarro et al. (2019) presented a promising, potentially calibration-free, approach to estimate the significant wave height from incoherent radar and applied it to study wave heights on a coral reef (Navarro et al., 2021).

Another approach that has been used in nearshore remote-sensing is to estimate wave dissipation instead of trying to measure the wave height. Wave dissipation indicates a loss of wave energy and directly influences many nearshore processes such as turbulence production and wave-induced currents. A proxy for wave dissipation is the presence of surface rollers, that is, the turbulent air-water mixture sliding down the front faces of breaking waves.

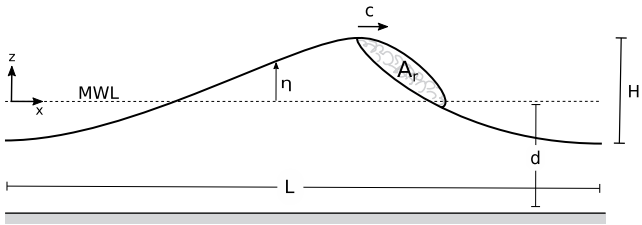

Figure 1. Illustration of the cross-section of a breaking wave carrying a surface roller with cross-sectional area A_r. Shown is the local surface elevation η, that is, the location of the free surface with respect to the mean water level (MWL). H is the wave height measured from crest-to-trough, L and d are wave length and mean water depth. The wave crest moves at the wave phase speed c in the positive x-direction.

One option is the assimilation of the frequency of occurrence of rollers, that is, the breaking probability, into parameterizations of the dissipation by depth induced breaking (Carini et al., 2015; Díaz Méndez et al., 2015). Another, more direct approach is to measure geometrical roller properties and approximate dissipation as the work done by the Reynolds stress at the roller/wave interface balancing the tangential weight of the roller (Duncan, 1981). Figure 1 shows a sketch of a breaking wave carrying a surface roller. The roller concept has been applied to time-averaged video (Aarninkhof & Ruessink, 2004), or more recently to thermal images (Carini et al., 2015), a combination of visible video and radar (Díaz et al., 2018; Flores et al., 2016), and scanning lidar data (Martins et al., 2018).

Within the present paper, we propose a new approach to apply the roller concept to Doppler radar data recorded by a shore-based, coherent-on-receive X-band marine radar. Preliminary results of this work were presented by Streβer and Horstmann (2019). Unlike camera based methods, which estimate dissipation based on geometrical roller properties, the proposed method is based on roller kinematics. More specifically the increase from slow to fast surface speeds at the toe (the front edge) of the surface roller is related to roller energy and dissipation. It can be obtained from the Doppler velocity measured by the radar. The method is used to efficiently obtain mean dissipation rates with relatively high spatial resolution (7.5 m) along a cross-shore transect spanning the entire surf zone (>1 km) of a double-barred, sandy beach.

The paper is structured as follows: The field measurements are described in Section 2. In Section 3, a scaling to obtain dissipation from the Doppler velocity is derived based on the concept of surface rollers. It is used to compute the evolution of radar-derived roller dissipation during a 3-day storm event is validated empirically through a comparison to the in-situ observations, and the sensitivity to the calibration parameters and the expected uncertainty are discussed. In Section 4, the cross-shore transformation of the wave height is presented and the performance of the method is studied by comparing it to in-situ measurements and simulations, and the consequences of the assumptions and simplifications are discussed. A general discussion of the advantages and limitations, as well as the transferability of the proposed methods to other sites and conditions is provided in Section 5, and an exemplary application is shown. Finally, a conclusive summary is given in Section 6.

2. Field Observations at Bunkerhill Beach, Sylt

The field measurements used for the present study were conducted from 27 Sep to 1 Oct 2016. The study area is located at Bunkerhill beach on the German North Sea island Sylt. Sylt is located close to the border between Germany and Denmark, and is the northernmost of the German barrier islands separating the Southern North sea from the intertidal flats of the Wadden Sea. The measurements were obtained at the West coast of the island in front of a long-term radar station operated by the Helmholtz-Zentrum Hereon. The beach can be classified as sandy, submesotidal, mixed-energy beach (equally influenced by tidal currents and wave action) with a median grain size of $D_{50} = 0.55$ mm (LKN.SH, 2015).

At the study site, the coastline is oriented at a small inclination of 2° with respect to North. The local coordinate reference system used in this paper has the origin at the location of the radar station (54.7903°N, 8.2833°E). The x- and y-axis are pointing toward East and North, respectively. The beach topography at the study site is shown in Figure 2. The subtidal region is composed of tide-corrected and quality-checked bathymetric data constructed from single-beam echo soundings recorded between Sep 22 and 26, 2016 (Cysewski et al., 2019). For the shown 2 km long stretch of the coastline, the subtidal bathymetry is uniform in the alongshore direction. The intertidal area and the dry beach are covered by airborne lidar data acquired on 26 Sep 2016, by the state of Schleswig-Holstein's Government-Owned Company for Coastal Protection, National Parks and Ocean Protection (LKN.SH). The data are mapped to a 5×5 m grid along the cross-shore transect in front of the radar station by averaging all data points within one grid cell. The cross-shore beach profile shows a subtidal sandbar with the crest located at $x = -500$ m at a vertical elevation $z \approx -4.5$ m-MSL, and an intertidal bar at $x = -160$ m and $z \approx -0.5$ m-MSL. The shoreline at a normal high water is at $x \approx -100$ m.

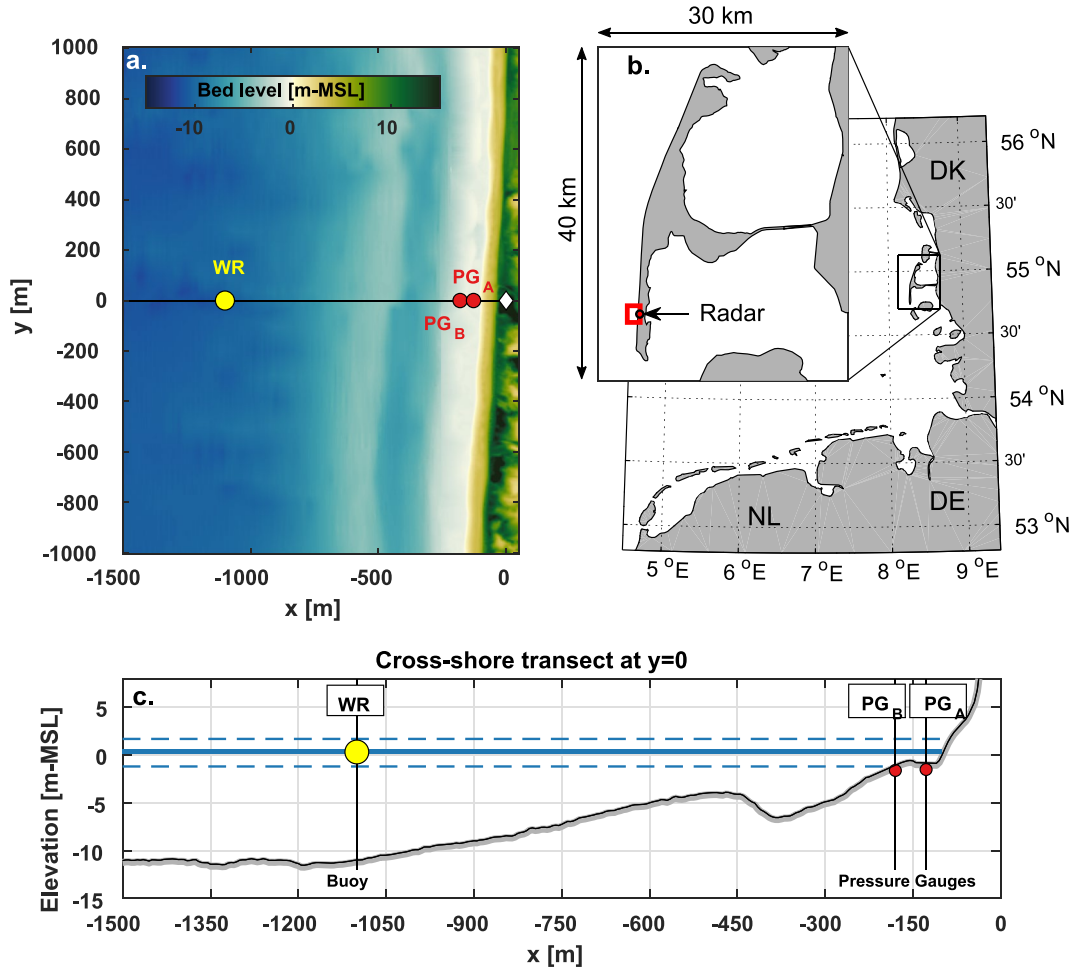

Figure 2. (a) Bathymetry with locations of the Doppler radar (white diamond), the wave rider buoy (yellow dot) and the bottom mounted pressure gauges (red dots). (b) Map showing the location of study region in the German Bight and a closer view to the Island Sylt with the location and extent of the study site. (c) Cross-shore transect at $y = 0$ m. The blue lines indicate the mean (solid), and minimum/maximum (dashed) water level during the field campaign.

The incident wave field is available from a wave rider buoy (a Datawell DWR-MkIII) located at $x = -1{,}100$ m. Two bottom mounted pressure transducers (Measurement Specialties 86BSD-050PA) were deployed in the intertidal region to provide wave height measurements at the inner bar. The first pressure gauge (PG_A) was located at the trough of the inner bar at $x = -127.5$ m and provided data until Sep 30. The second (PG_B) provided data for the entire study period and was located at $x = -180$ m, which is ≈30 m offshore of the bar crest. The pressure signal was logged at 10 Hz and transformed to surface elevation η_{PG} using the weakly nonlinear method of Bonneton et al. (2018) after smoothing the raw time series with a 5-point (0.5 s) moving average filter and removing the mean hydrostatic water level and a linear trend (due to tides) in segments spanning 30 min η_{PG} thus represents the time-varying deviation of the free surface from the mean water level (MWL) as indicated in Figure 1. On recovery, the pressures gauges were immersed into the sand by ≈ 30 cm. There are no time varying measurements of the burial depth available. To estimate the error due to burial, the surface elevation variance was estimated assuming the sensor at the sea bed, and 30 cm below the bottom level (by applying Equation 5 of Raubenheimer et al., 1998, in the frequency range between 0.05 and 0.33 Hz). For this limiting case, the surface elevation variance was underestimated by 13% (median value). Water elevation and currents due to the tide and surge, as well as the 10-m wind speed are available from the operational model BSHcmod (Dick, 2001) operated by the ”Bundesamt für Seeschiffahrt und Hydrographie” (BSH), the German federal hydrographic and maritime traffic agency. Deviations from the true surface elevation during the bathymetry measurements were below 0.15 m, indicating a reasonable accuracy of the operational model for the purpose of the present study.

The sea state is mostly locally generated and grows rapidly from 0.5 m to ≈2 m significant wave height on the second half of Sep 27. Simultaneously, the peak wave period increases from 4 s to around 8 s. While wave periods remain constant around 8 s on Sep 28, they increase further on Sep 29 reaching a maximum of 10.5 s on Sep 30, 01:00 UTC. The maximum significant wave height of 3.3 m is reached a little earlier, on Sep 29, 23:00 UTC, and remained constant on this level for 3 hr. Afterward, the significant wave height decreases rapidly to 2 m on Sep 30, 03:00 UTC. During the following 24 hr it drops further to a level of about 1 m on Oct 1, 03:00 UTC. Throughout the entire storm, wind speeds and significant wave heights are highly correlated indicating a young, locally generated sea state. Both waves and winds during the storm were directed onshore, mostly approaching from the West, with peak wave incidence angles deviating up to 40° from shore normal, while the vast majority (>75%) of the dataset shows incidence angles below 25° from shore normal.

2.1. Coherent X-Band Radar Measurements

2.1.1. Radar Hardware

The radar used in this study is a coherent-on-receive marine radar developed at the Helmholtz-Zentrum Hereon (Hereon, formerly Helmholtz-Zentrum Geethacht, HZG) in collaboration with the Saint Petersburg Electrotechnical University (ETU-LETI). A detailed description of Hereons marine radar is given by Horstmann et al. (2021). The radar system consists of an off-the-shelf X-band (9.48 GHz) marine radar (GEM Leonardo series). Dedicated electronics were added for the digitization and coherentization of the radar signal. The radar is also equipped with a step-motor, which allows the operator to steer the antenna in a fixed pointing direction or to run it in the standard rotating antenna operation mode. For the present study, the radar was equipped with a 7.5 feet (≈2.2 m) antenna vertically polarized in transmit and receive (VV). It was located approximately 28 m above sea level. The pulse repetition frequency (PRF) was set to 2 kHz with a duration of the transmitted pulses (measured at the half power level) between 50 and 70 ns. Analog-to-digital conversion was realized at 80 MHz and then subsampled to 20 MHz corresponding to a sampling range cell spacing of 7.5 m. A total number of 435 range cells were sampled resulting in a maximum range of roughly 3.2 km.

2.1.2. Doppler Signal Processing and Interpretation

Coherent radar measures the amplitude and phase of the received radiation. It facilitates the measurement of the Doppler frequency shift f_D, which is induced by relative motions of the backscattering elements, the scatterers, with respect to the radar antenna. The corresponding Doppler velocity U_D is related to the Doppler frequency shift through the well known Doppler equation:

$$U_D = \frac{f_D \lambda_{el}}{2 \cos \alpha}, \tag{1}$$

where λ_{el} is the electromagnetic wave length of the radar signal and α is the projection angle between the scatterer motion and the line-of-sight of the antenna. For the present study, the radar antenna was static, pointing in the cross-shore direction at grazing angles below 10° for the vast majority of the dataset. The Doppler velocity thus represents the cross-shore component of the horizontal scatterer velocity. For X-band radar, the main backscatter from non-breaking parts of the surface is due to Bragg-resonance at the scale of half the radar wave length; hence, the radar measures the horizontal speed of these so called Bragg waves. However, there are further contributions to the Doppler velocity that can complicate its geophysical interpretation. The Doppler velocity may be interpreted as a sum of various components:

$$U_D = U_{Bragg} + U_{curr} + U_{drift} + U_{orb} + U_{break} + U_{graz}, \tag{2}$$

where U_{Bragg} is the Bragg waves' phase speed, U_{curr} is the mean current, U_{drift} is the a drift velocity due to wind shear and Stokes drift, U_{break} is the contribution of breaking waves, and U_{graz} is an additional Doppler shift apparent at grazing incidence. The reason for this additional Doppler shift U_{graz} is still not well understood. It involves complicated interactions of steep waves and shadowing at spatial scales smaller than the radar resolution (Miret et al., 2014), or pulse-smearing artifacts (Streβer et al., 2021). The speed of the Bragg waves U_{Bragg} is constant. In the nearshore, wave induced circulation and changing wave heights can cause considerable variability of U_{curr} and U_{drift} over the distance covered by the radar (3 km) and for the typical duration of a radar record (10 min for the present study). However, the variability at the scale of the radar resolution $\mathcal{O}$(10 m/1 s) is mainly due to

the wave orbital motions U_{orb} and the contribution due to breaking U_{break}. At breaking, the scatterer speed U_{break} is related to parasitic capillary waves at the steep front faces or, for the actively breaking parts, the water mass that is accelerated horizontally in the breaking process. This can be either the plunging jet of water that forms at incipient breaking or, for spilling breakers, the water particles in the turbulent aerated region at the font face of the breaker, that is, the surface roller. The roller is moving at a much faster speed than the non-breaking surface in front of it, and the magnitude of this spatial difference in scatterer velocity can be used to infer dissipation. This is described in detail in the following Section 3.

To estimate the Doppler velocity, Doppler spectra were computed from the complex coherent radar signal for short ensembles of $n = 1{,}024$ consecutive radar pulses. The integration time of one Doppler measurement is thus $dt = 0.512$ s (at PRF = 2,000 Hz). The Doppler shift frequency f_D is determined from the location of the Doppler peaks along the frequency axis as described by Streβer et al. (2021). In some cases, multiple peaks are found in the Doppler spectra. This can happen if breaking waves only partially fill a radar cell, but also due to the leakage of pulse energy into adjacent range cells, in particular behind the breaking crests. For such multi-peaked spectra, only the slowest peak is considered. The velocity of the slower peaks was found to be best suited to trace the non-breaking surface with only minor influence of radar pulse smearing artifacts (Streβer et al., 2021).

3. Radar-Derived Dissipation

The primary goal in the present work is to find a relationship between the Doppler radar observations and wave energy dissipation. Microwave radar is very sensitive to the presence of breaking waves and the surface rollers carried by them. When a roller is present within a radar ground cell, the backscatter intensity is significantly increased (e.g., Catalán et al., 2011, 2014; Farquharson et al., 2005). There have been some attempts to relate the observed backscatter either to roller dimensions estimated with the physical optics approximation for scattering from a smooth cylinder (Farquharson et al., 2005) or to the portion of the radar footprint occupied by breakers (Haller & Lyzenga, 2003). A universal model for the radar cross section (RCS) associated with actively breaking waves is still not available. Moreover, relating the observed backscatter intensity to RCS requires radiometric calibration for each individual radar, which requires significant effort and is usually not being performed. For this reason we describe a method based on the Doppler velocity rather than RCS.

For actively breaking waves, the radar backscatter originates from the droplets inside the surface roller (e.g., Catalán et al., 2014). Those are moving relatively fast, roughly at the phase speed c of the wave carrying the roller. In the absence of breaking, a much slower scatterer speed is expected, that is closer to the waves' orbital velocity (cf. Section 2.1.2). Therefore, when the waves are traveling toward the radar, a large increase of the Doppler velocity is expected at the transition from non-breaking to actively breaking parts of the sea surface at the front edge (the toe) of the roller (as visualized in Figure 1). If the difference $dU = U_{D,ri+1} - U_{D,ri}$ of the Doppler velocity at the range cell $ri + 1$ and the preceding range cell ri is positive and large, this most likely indicates the transition from non-breaking to breaking parts of the surface. The wave energy dissipation due to wave breaking is related to the vertical velocity shear. It is determined by the velocity difference between water particle velocity at the surface (within the roller) and the underlying water mass (e.g., Svendsen, 1984). Our hypothesis is thus that the large positive spatial Doppler velocity difference dU observed at the toe of surface rollers can be used as a proxy for this horizontal velocity shear and is linked to energy dissipation.

In the following, a physically motivated scaling that relates dU to wave dissipation is derived. It is based on the roller concept and relies on the assumption, that the spatial difference in Doppler velocity $dU = U_{D,ri+1} - U_{D,ri}$ of the Doppler velocity at the range cell $ri + 1$ and the preceding range cell ri can be used to approximate the breaking phase speed, hence:

$$c = \beta_D \, dU. \tag{3}$$

This is a reasonable assumption, because the horizontal orbital velocity at the radar cell just before the front edge of the roller is likely to be small. For the next radar cell, which is dominated by the roller, the Doppler velocity is close to the phase speed of the breaking wave. The parameter β_D can be used to correct for systematic errors in the relationship between c and dU. For waves traveling toward the radar antenna, dU will always be positive at the roller toe. On the contrary, a negative difference is expected at the transition from breaking to non-breaking. However, Streβer et al. (2021) showed that radar pulse smearing can lead to signal artifacts at the rear sides of

steep and breaking waves. There is a high chance that Doppler velocity observed in this region is invalid. Therefore, only the positive differences $dU > 0$ are considered here and all negative differences are excluded from the computations.

3.1. Surface Roller Properties

For long-crested waves, the total (bulk) kinetic energy stored in the surface roller per unit span is given by

$$E_{r,total} = \frac{1}{2}\rho' A_r \left(\overline{u_r^2} + \overline{w_r^2}\right), \tag{4}$$

where A_r is the cross-sectional roller area, u_r and w_r are the bulk horizontal and vertical motions of the roller and the overbar indicates time averaging. The bulk density of the roller, including both water and air, can be expressed as

$$\rho' = \beta_\rho \, \rho_w, \tag{5}$$

where β_ρ represents the reduction of the water density ρ_w according to the void fraction inside the roller. The void fractions in the roller region show substantial variability during different phases of the breaking process (Kimmoun & Branger, 2007; Rojas & Loewen, 2010). A default value of $\beta_\rho = 0.9$ was selected here, which was shown to be a reasonable assumption by Martins et al. (2018) who used 0.87, and it is close to unity, which is the value often used in earlier studies (e.g., Deigaard & Fredsøe, 1989). Phase-averaging the total roller energy yields the roller energy per unit area

$$E_r = \frac{E_{r,total}}{L}, \tag{6}$$

where L is the wave length. Since the roller remains in the region between the wave crest and the MWL, the vertical component of the roller motion is small ($w_r \ll u_r$) and the roller moves horizontally with the same speed as the breaking wave; hence:

$$\left(\overline{u_r^2} + \overline{w_r^2}\right) \approx c^2. \tag{7}$$

The roller area can be expressed as

$$A_r = \kappa \, HL, \tag{8}$$

where H is the wave height and κ is a proportionality constant that varies between 0.06 and 0.07 (Okayasu et al., 1986; Svendsen, 2005). Although Martins et al. (2018) note that this relation most likely overestimates the roller area and other scalings exist in the literature (see Table 2 of Martins et al., 2018), Equation 8 is selected here because it provides the advantage that the wave length can be eliminated from Equation 6. Combining Equations 4 and 6–8 yields for the roller energy

$$E_r = \frac{1}{2} \, \rho' \, \kappa \, H \, c^2. \tag{9}$$

The wave height cannot be measured directly by the radar. To substitute H, the dependency of the shallow water wave propagation speed on the wave height (amplitude dispersion) is exploited using an empirical predictor similar to the one proposed by Hedges (1976) for the nonlinear shallow water phase speed

$$c = \sqrt{g(d + \alpha_{ad} H)}, \tag{10}$$

where g is the Earth's gravity and d is the water depth. The calibration coefficient α_{ad} determines to what extent the amplitude dispersion is considered. For $\alpha_{ad} = 0$, Equation 10 corresponds to the shallow water phase velocity according to linear wave theory, whereas for $\alpha_{ad} = 1$ it corresponds to solitary wave theory. As suggested by Booij (1981), $\alpha_{ad} = 0.5$ was selected as a default since higher values will most likely overestimate the shallow water phase speed. The water depth at the breakpoint can be roughly estimated as

Table 1
Dimensionless Calibration Parameters for the Scaling of the Radar-Derived Roller Properties

Parameter	Symbol	Default value	Expected range
Relative roller density	β_ρ	0.9	[0.3, 0.9]
Roller area scaling factor	κ	0.07	[0.06, 0.07]
Breaker parameter	γ	0.78	[0.4, 0.88]
Amplitude dispersion factor	α_{ad}	0.5	[0.0, 1]
Breaker slope parameter	β_s	0.1	[0.05, 0.15]
dU to c conversion factor	β_D	1	[0.7, 1.3]

$$d = \frac{H}{\gamma}, \tag{11}$$

where γ is the well known breaker parameter. A default value of 0.78 was selected which is often used for practical purposes and is well in the range of the values observed in the field (e.g., Carini et al., 2021b), although on average the reported values were slightly smaller. Combining Equations 10 and 11 yields the approximate expression

$$H = \frac{c^2}{g\left(\frac{1}{\gamma} + \alpha_{ad}\right)}, \tag{12}$$

relating the wave height of a breaking shallow water wave to its phase speed. Combining Equations 3, 9 and 12 finally yields a scaling for the roller energy as a function of the phase speed c of the breaker

$$E_r = \frac{\beta_\rho\, \kappa\, \rho_w}{2g\left(\frac{1}{\gamma} + \alpha_{ad}\right)} c^4. \tag{13}$$

Equations 13 and 3 provide the basis to obtain roller properties from the Doppler velocity. To provide a more convenient scaling for the radar-derived roller properties, all calibration parameters within Equation 13 are combined to one single scaling factor $B_r = \beta_\rho\, \kappa \left(2\left(\gamma^{-1} + \alpha_{ad}\right)\right)^{-1}$ and the final scaling for radar-derived roller energy reads

$$E_r = B_r \frac{\rho_w}{g} \overline{(\beta_D\, dU)^4}, \tag{14}$$

where the over-bar indicates time averaging over the full radar record (10 min for the present study). Accordingly, the flux of roller energy is given by

$$F_r = E_r\, c = B_r \frac{\rho_w}{g} \overline{(\beta_D\, dU)^5}. \tag{15}$$

The dissipation of roller energy is related to the roller energy through

$$D_\tau = \frac{2 E_r g \beta_s}{c}, \tag{16}$$

where β_s is the slope at the inner interface between the roller and the underlying water body (Deigaard & Fredsøe, 1989; Nairn et al., 1991). Therefore, the scaling for the roller dissipation derived from the radar is

$$D_\tau = 2\, B_r\, \rho_w\, \overline{(\beta_D\, dU)^3}\, \beta_s. \tag{17}$$

The commonly used default value of 0.1 was selected for β_s.

All calibration parameters that affect B_r are listed in Table 1. The assumed default values and the expected minimum and maximum values are also listed for each parameter. The default value for the radar roller dissipation scaling factor is $B_r = 0.0177$. Given the expected ranges of each calibration factor (shown in Table 1) contributing to B_r, this factor is expected to range within 0.0026 and 0.027. The implications of this parameter range for the expected accuracy of the proposed method are discussed in detail in Section 3.3.

Figure 3 shows the radar-derived mean roller dissipation D_τ (Equation 17) over the course of the storm. The mean roller dissipation was computed from the hourly 10-min long radar measurements collected in the static antenna mode. Also shown is the significant wave height H_s observed by the wave rider as well as the mean water elevation extracted from the operational model BSHcmod of the German federal hydrographic and maritime traffic agency, that includes the astronomical tide and wind induced surge. Rollers are present at the outer bar (-800 m $< x < -350$ m) during low tides when $H_s > 1.5$ m. At the peak of the storm, when wave heights reach up to 3 m, the outer bar also remains active during high tide and roller dissipation rates at the crest of the outer bar

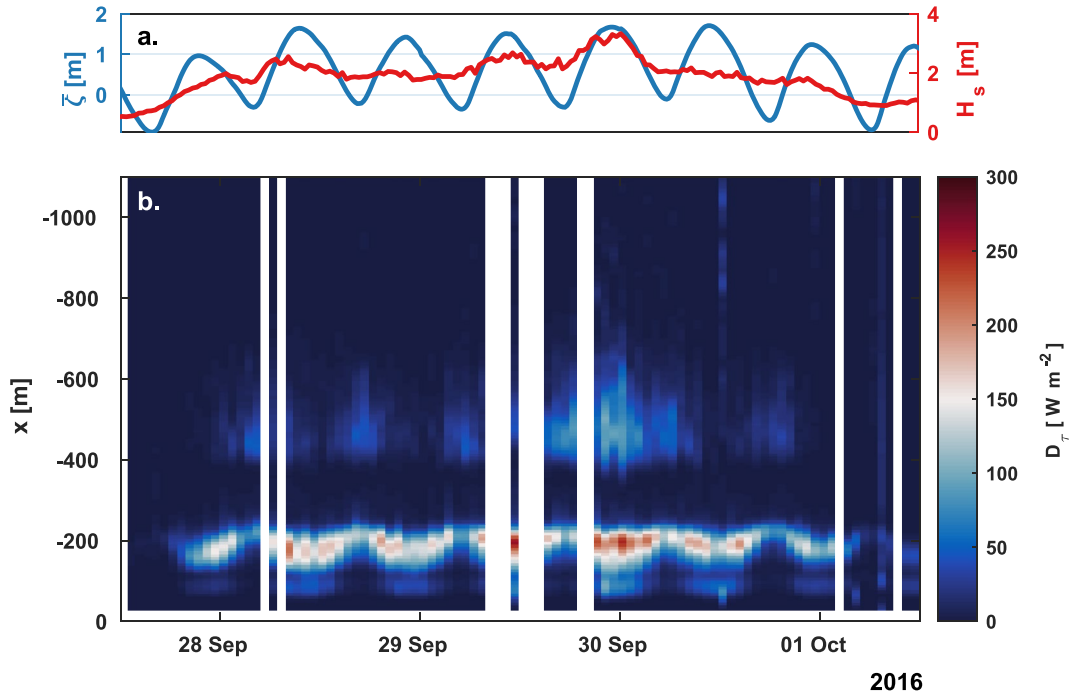

Figure 3. (a) Significant wave height H_s observed by the wave rider buoy and the mean water elevation ζ (tide + surge) from the operational model BSHcmod. (b) Time-space evolution of radar-derived roller dissipation averaged over 10 min at the beginning of each hour.

($x = -500$ m) reach up to ≈120 W m^{-2}. At the inner bar ($x \approx -200$ m, depending on the tide), roller dissipation rates are generally higher and reach values >200 W m^{-2} over a relatively short distance of less than 100 m. Both the location and the extent of the inner breaker zone are strongly modulated by the tide. It moves further offshore at low tide when its cross-shore extent is significantly narrower than at high tide. In the swash zone right at the beach face ($x \approx -90$ m), rollers are only present at high tide, when the crest of the inter-tidal bar is submerged allowing some wave energy to pass.

3.2. Empirical Assessment

To carry out an in depth validation, in-situ measurements of dissipation at several location along the cross-shore transect would be needed. As this is not available for the present dataset, the radar derived dissipation D_τ (Equation 17) was compared to dissipation estimated from the pressure gauges, as a first step toward a validation. The bulk dissipation between the pressure wave gauges is computed from the wave energy flux gradient as

$$D_{PG} = \frac{F_{PG_B} - F_{PG_A}}{|x_{PG_B} - x_{PG_A}|}, \tag{18}$$

where x_{PG_A} and x_{PG_B} are the cross-shore location of the pressure gauges and F_{PG_A} and F_{PG_B} the wave energy flux at each pressure gauge evaluated for 30 min lasting ensembles of pressure readings. Assuming that the potential and kinetic energy of the wave motion are equal, the wave energy flux was computed as

$$F_{PG} = \rho_w g \overline{\eta_{PG}^2} c_g, \tag{19}$$

where η_{PG} is the surface elevation obtained from the pressure gauges (see Section 2), ρ_w is water density, and c_g is the group speed of the waves, which was determined from linear wave theory considering the peak period measured at the buoy and the local water depth obtained from the mean pressure. Since η is defined as the deviation from the MWL (see Section 2, and Figure 1), $\overline{\eta_{PG}^2}$ is the surface elevation variance in a pressure ensemble (30 min). The comparison yielded a root-mean-square deviation (RMSD) between the D_τ and D_{PG} of 18.12 W m−2, and a normalized root-mean-square deviation (NRMSD) of 26% (normalized by the mean value of D_{PG}).

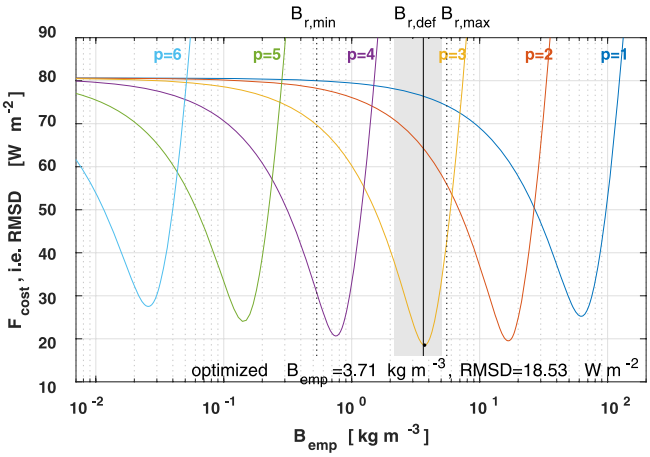

Figure 4. Visualization of the cost function (representing the root-mean-square deviation) for different exponents p to optimize the empirical scaling factor B_{emp} against the dissipation estimated from the flux gradient between the pressure wave gauges. $B_{r,def}$ (vertical solid line), $B_{r,\min}$ and $B_{r,\max}$ (vertical dashed lines) are respectively the default, minimum, and maximum value for the scaling factor estimated from the expected parameter range for the physical scaling. The gray area indicates $B_{r,def}(1 \pm 40\%)$.

The physically motivated scaling derived in Section 3.1 involves multiple strong assumptions and approximations. Therefore, the following independent empirical power-law was also tested against the data:

$$D_{emp} = B_{emp}\,\overline{dU^p}, \tag{20}$$

where B_{emp} and the exponent p are calibration constants and the overbar indicates time averaging over the 10 min long radar record. To determine the empirical constants B_{emp} and p, a cost function is computed representing the RMSD between the radar estimate and the observations:

$$F_{cost}(B_{emp}, p) = \sqrt{\frac{\sum_{n=1}^{N}(D_{emp,n} - D_{PG,n})^2}{N}}, \tag{21}$$

where $N = 52$ is the total number of available measurements where the radar and both pressure gauges provided valid data. Resulting from dimensional analysis, the unit of B_{emp} must be [kg m^{-3}] to correctly fit to the unit of dissipation [W m^{-2}]. Note, that the empirically derived dissipation rate D_{emp} (Equation 20) was evaluated two radar range cells (15 m) further offshore than the location of the pressure gauges. This is needed because the jump from slow to fast scatterers appears at the toe of the surface roller, but the point where the wave energy is dissipated (the wave crest) is located slightly further offshore. For now, only integer values in the range of [1,5] were tested for the exponent p. The resulting F_{cost} for the different p is shown in Figure 4. It can be seen that the minimum of F_{cost} is found for $B_{emp} = 3.71$ kg m^{-3} and $p = 3$, where the RMSD from the observations was 18.53 W m^{-2}. However, neighboring exponents do not result in significantly larger RMSDs (19.51 W m^{-2} for $p = 2$, 20.64 W m^{-2} for $p = 4$) confirming the strong link between the spatial increase of the Doppler velocity dU and wave dissipation. Figure 4 also gives an idea about the sensitivity of the method to different values of B_r. The RMSD at the borders of the gray area, which indicates $B_{r,def}(1 \pm 40\%)$, is still below 37 W m^{-2} corresponding to a NRMSD of ≈50%. This suggests that a reasonable accuracy of the method is achieved if B_r is estimated within 40% of the optimal value.

In order to compare the default value for the physically motivated scaling parameter B_r introduced in Section 3.1 to the optimized empirical calibration parameter B_{emp}, it was transformed to a dimensional form considering Equation 17 as $B_{r,def} = 2\,B_r\,\rho_w\,\beta_s$, where $\beta_s = 0.1$ is the same slope parameter as used in Equation 17. Similarly, the equivalent lower and upper limits $B_{r,\min}$ and $B_{r,\max}$ were determined. The resulting equivalent scaling parameters are $B_{r,def} = 3.63$ kg m^{-3}, $B_{r,\min} = 0.53$ kg m^{-3} and $B_{r,\max} = 5.54$ kg m^{-3}. These are shown in Figure 4 as vertical lines. The equivalent default value $B_{r,def} = 3.63$ kg m^{-3} is very close to the optimized value $B_{emp} = 3.71$ kg m^{-3}, which shows that Equation 17 and Equation 20 are basically identical and thus they both provide the same estimate for D_τ. The similarity between the two approaches supports the assumptions involved in the physically motivated scaling based on roller concept (Equation 17). However, the empirical scaling (Equation 20) does not rely on any assumptions apriori and thus it may be seen as a more universal approach to the problem without the restrictions that come with the roller concept. This is further discussed in Section 5.2.

3.3. Uncertainty

For the physically motivated scaling for the roller energy (Equation 14) and roller energy flux (Equation 15) errors may result from uncertainty in the correct choice of the calibration parameter B_r and the correction parameter β_D to adjust the relationship between dU and c. The radar derived roller dissipation (Equation 17) is further affected by the uncertainty of the roller slope parameter β_s. Recently, the use of lidar for studying surf zone wave shapes and wave kinematics brought important insights regarding some relevant quantities such as the height to depth ratio or the front slope of breaking waves (Carini et al., 2021a; Martins et al., 2018). However, both quantities show a substantial variability even for the same beach and wave characteristics. Moreover, the roller concept must be seen as a means to simplify the complex dynamics of breaking waves. Many of the parameters involved, such as the roller area, relative roller density, and the inner roller slope at the interface between the roller and

the underlying water, are not clearly defined in reality and thus difficult to determine from field observations. For example, as noted by Martins et al. (2018), the density and area of the roller are directly linked through the definition of the roller itself. Therefore, the combined scaling factor B_r should be rather interpreted as a general physically motivated calibration parameter for the proposed method rather than a quantity that could be derived from additional observations. Nonetheless, the expected range of B_r considering typically used parameters as described in 3.1 can be used to provide a rough estimate of the expected uncertainty.

As mentioned in Section 3.1, the default value of the radar roller dissipation scaling factor B_r is 0.0177, and the estimated lower and upper bounds are 0.0026 and 0.027, respectively. This corresponds to a relative deviation from the expected default value of 85% for the lower limit and 53% for the upper limit. The second source of uncertainty stems from the parameter β_D. For the present study, β_D was set to one implying the assumption $dU = c$. However, environmental conditions such as the sea state, the wind and also the radar installation height may affect the correct choice of β_D. A systematic analysis of the dependency of β_D on these external factors may result in a reduction of uncertainty in future. The expected range of β_D from 0.7 to 1.3 implies an error of $\pm$30% for the estimation of wave phase speed (i.e., $c = (1 \pm 0.3)\, dU$). Since the dissipation scales with dU^3 (see Equation 24), error propagation yields an uncertainty of 90% for *individual* measurements of the dissipation. However, for the mean dissipation over one 10-min radar record, this error will be significantly reduced due to averaging. The integration time of 0.512 s for the Doppler velocity yields $N = 1{,}170$ measurements of dU during the 10-min sampling. If all measurements were independent and there was no bias, the error would be reduced by a factor of $1{,}170^{-0.5}$ resulting in an approximate relative error for the mean dissipation and roller energy of 2.6% and 3.5%, respectively. However, it is unlikely that all measurements of dU are independent particularly if they belong to the same individual wave. A better assumption could be to consider the number of waves in the record instead of the number of samples. The peak period measured by the wave rider buoy is 10 s meaning approximately 60 waves are observed during a 10-min long radar record. This translates to an estimated relative uncertainty due to variability in β_D of 11.6% for the mean dissipation and 15.5% for the roller energy, which adds up to the uncertainty due to B_r.

This theoretical assessment suggest a potentially large total uncertainty for the method which is in the order of 100%. However, the empirical assessment (Section 3.2) revealed an observed NRMSD of $\approx$26%, suggesting a much smaller uncertainty at least for the wave conditions covered. This could be due to the fact that, either the expected range of B_r is considerably smaller than expected, or that the different sources of error compensate each other, which is something that should be investigated in future studies involving further data sources.

4. Cross-Shore Transformation of Wave Height

Wave heights in shallow water are strongly influenced by the local water depth. Therefore, the skill of numerical models in predicting nearshore wave heights depends to a large extent on the availability of an up-to-date bathymetry map as well as accurate information on the incident wave energy. This information is often not available and beach profiles can change rapidly, sometimes within a few hours in storm conditions. The proposed radar methodology to obtain roller energy flux and dissipation does not require any additional information. It is therefore interesting to further assess the performance of the radar in comparison to a numerical wave model under optimal preconditions, that is, a recent bathymetry is available and the incoming wave energy flux is known. The results are presented in terms of the significant wave height H_s (defined as 4 times the standard deviation of the surface elevation), which is expected to be more conceivable than the wave energy flux for most readers. The distribution of H_s along the cross-shore transect is computed for both the radar and the model using a coupled wave and roller energy flux balance as explained in the following.

4.1. Bulk Wave and Roller Energy Balance

For the simplified case of a stationary, unidirectional, normally incident, random wave field, and in the absence of cross-shore currents, the cross-shore wave momentum flux balance can be written as

$$\frac{\partial F_w}{\partial x} = -D_w, \tag{22}$$

where $F_w = E_w c_g$ is wave energy flux and $E_w = \frac{1}{16}\rho_w g H_s^2$ is the organized wave energy. The source term D_w is the bulk wave energy dissipation. For the present study, dissipation by breaking is the only source term considered. The consequences of disregarding other processes are discussed in detail in Section 4.3. Svendsen (1984) showed that surface rollers carry a large portion of the total momentum flux in the surf zone. This must be considered in the cross-shore momentum balance. The roller energy is transported toward shore at the phase speed c of the wave carrying the roller. Thus, the cross-shore balance of roller energy reads

$$\frac{\partial F_r}{\partial x} = D_w - D_\tau, \tag{23}$$

where $F_r = E_r c$ is the roller energy flux and D_τ is the dissipation of roller energy (Equation 16) and D_w is the wave energy dissipation from Equation 22. The wave dissipation couples Equation 22 with Equation 23. Once wave energy is dissipated, it is transferred to roller energy and is finally dissipated by the shear stress between the roller and the underlying water body. This generates turbulence and drives wave-induced currents. The roller energy grows or decays according to the difference of D_w and D_τ. Coupling the roller and wave energy balance in this manner was first proposed by Nairn et al. (1991) and, unlike Svendsen's original roller model, it causes a lag in the location where the total energy is dissipated.

The roller energy E_r, the flux of roller energy F_r, and the dissipation of roller energy D_τ can be directly estimated from the radar measurements using Equations 14, 15 and 17. The dissipation of organized wave energy D_w, at the location x_{ri+1} of the range cell $ri + 1$ is estimated numerically according to Equation 23 as

$$D_{w,ri+1} = \frac{F_{r,ri} - F_{r,ri+1}}{\Delta r} + D_{\tau,ri}, \tag{24}$$

where $\Delta r = x_{ri+1} - x_{ri}$ is the distance between two adjacent radar range cells (here 7.5 m). The wave energy flux at x_{ri+1} then follows from Equation 22 as

$$F_{w,ri+1} = F_{w,ri} + D_{w,ri}\ \Delta r, \tag{25}$$

and the wave energy and significant wave height along the full radar transect are given by

$$E_{w,ri} = \frac{F_{w,ri}}{c_{g,ri}} \tag{26}$$

and

$$H_{s,r_i} = \sqrt{\frac{16\ E_{w,r_i}}{\rho_w\ g}}. \tag{27}$$

The energy flux at the beach is initialized as zero, hence any reflection of wave energy at the shoreline is neglected which is a reasonable assumption at the present beach (as shown in Section 4.3). The first order numerical integration scheme used in Equation 25 is sensitive to large gradients. Since the radar observations naturally involve some high frequency noise, the radar-derived roller energy (Equation 14), the flux of roller energy (Equation 15) as well as the dissipation of roller energy (Equation 17) were smoothed with a moving average filter spanning five range cells to avoid unrealistically high gradients. The results for the wave height is qualitatively similar if the unsmoothed values are used (not shown), but the smoothing leads to smaller dissipation estimates in the swash zone. This causes a negative bias of roughly 10 cm for the estimated wave heights offshore of the swash zone.

For comparison to the radar results, the cross-shore wave and roller energy and dissipation was also simulated numerically by solving Equations 22 and 23 in the opposite direction, that is, starting offshore. The incoming flux of wave energy at the offshore boundary was derived from the wave rider buoy and the wave dissipation D_w was estimated using the parameterization proposed by Janssen and Battjes (2007) (referred to as JB07, further details can be found in Appendix A).

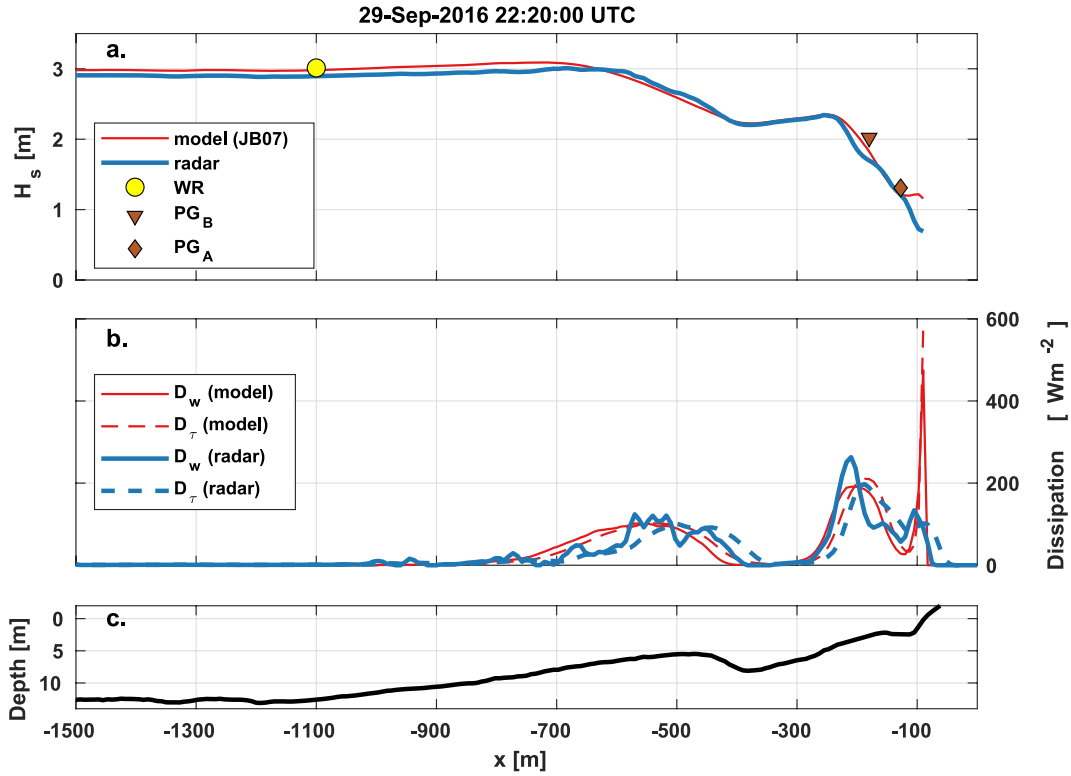

Figure 5. Top: Cross-shore transformation of the significant wave height H_s at the peak of the storm (29 Sep 2016 22:20 UTC) as observed by the radar (blue) and simulated with the parameterization of Janssen and Battjes (2007) (JB07, red). Also shown are in-situ observations at the wave rider buoy (WR, yellow circle) and the pressure gauges PG_B (brown triangle) as well as PG_A (brown diamond). Center: Observed (blue) and simulated (red) dissipation of organized wave energy D_w and roller dissipation D_τ. Bottom: Depth profile at the time of the measurements.

4.2. Comparison With Observations and Model Results

Figure 5 shows the cross-shore transect of the significant wave height derived from the radar observations (blue line) and the model (red line) at the peak of the storm event, when the offshore significant wave height was 3.2 m with a peak period of 10 s. Also shown are the cross-shore distributions of observed and simulated wave and roller dissipation, as well as the beach profile. The H_s-profile obtained from the radar yields a realistic cross-shore distribution of H_s. It is very similar to the result from the simulation for this situation. The observed wave height at all available in-situ sensors, the pressure wave gauges PG_A and PG_B, and the wave rider buoy is matched well. The radar slightly underestimates the wave height that is observed at PG_B ($x = -180$ m), whereas the model seems to match the in-situ observations better at this location. The reason for this can be seen in the center panel of Figure 5. The wave dissipation rate D_w observed by the radar just offshore of PG_B ($\approx$280 W m^{-2}) is significantly higher than the one predicted by the model ($\approx$190 W m^{-2}). Accordingly, the radar-derived wave height decreases faster in this region compared to the simulation. The transition region after onset of breaking until the point when the rollers have formed is still not well understood and the assumption of an analogy between breaking waves and a moving bore within the JB07 parameterization is violated. It is therefore possible, that the radar observations provide a more realistic estimate for the wave dissipation in this transition region, but further ground truth with better spatial coverage would be needed to investigate this. However, it is interesting that the observed and the simulated roller dissipation D_τ in the region of the inner bar have similar magnitudes. This shows nicely that the formation of surface rollers compensates abrupt changes in organized wave energy leading to a smoothing and an onshore shift of the forcing of wave-induced currents (e.g., Goda, 2006).

To better quantify the overall performance of the proposed method, error statistics are computed for the locations where in-situ data is available. Figure 6 shows the time series of the observed and the simulated significant wave heights at the wave rider buoy (WR) and the two bottom mounted pressure wave gauges (PG_B and PG_A). Also shown are the corresponding scatter diagrams and error metrics. Both, the radar observations and the simulations

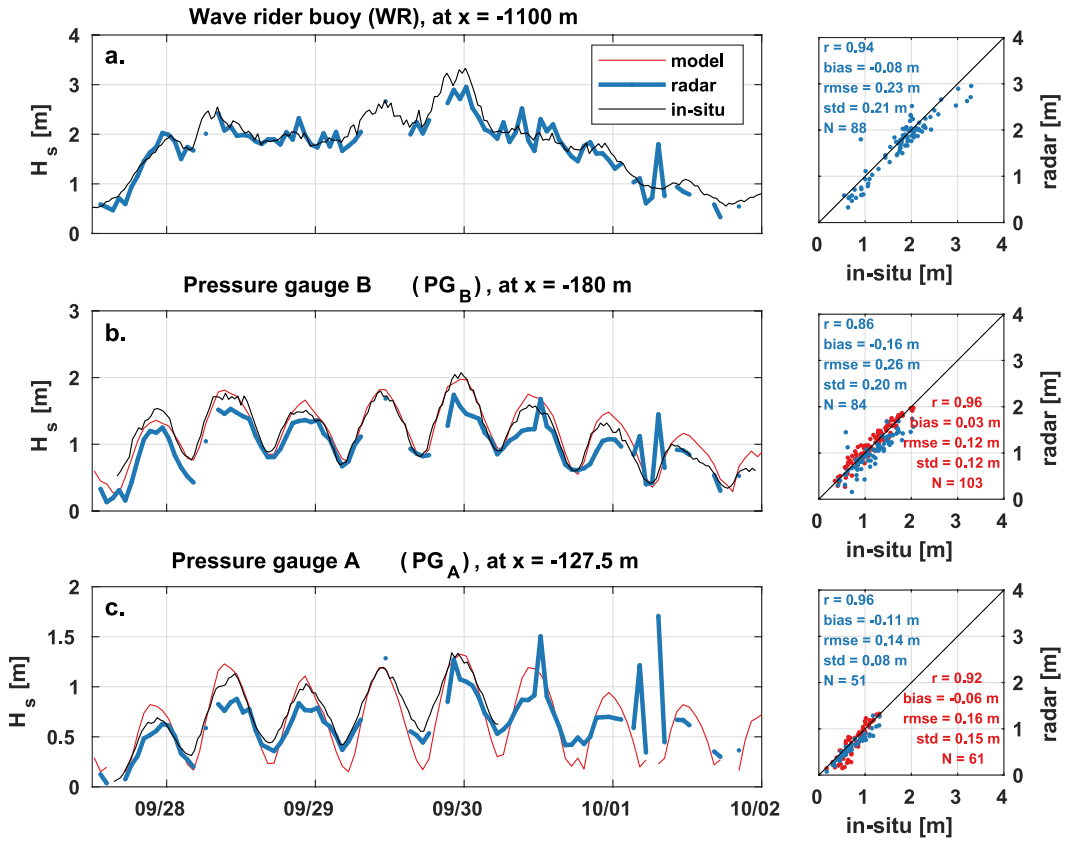

Figure 6. Time series of significant wave height observed by the radar (blue), simulated by the model (red) and in-situ observations (black) at the locations of the in-situ sensors, that is, (a) the wave rider buoy (WR), and the two bottom mounted pressure wave gauges PG_B (b) and PG_A (c). The right panels show the corresponding scatter diagrams of H_s and error statistics.

are matching the in-situ measurements well at all three locations throughout the entire storm event. The root-mean square errors (RMSE) and corresponding bias (in parenthesis) of the radar observations (blue colors) are 0.14 m (−0.11 m), 0.26 m (−0.16 m), and 0.23 m (−0.08 m), at PG_A, PG_B and WR, respectively. When normalized by the mean, this corresponds to normalized root-mean square errors (NRMSE) of 19%, 22%, and 13%, at PG_A, PG_B, and WR, respectively. The combined RMSE taking all available sensors into account is 0.22 m (NRMSE = 17%) and the overall bias is −0.12 m. The negative bias may be explained by the consequences of smoothing, but this should be investigated carefully in future experiments involving better resolved ground truth. While the results are generally very good during the growing phase of the storm, a slight decrease in the performance is apparent in the decaying phase. This can be explained by the presence of rain, which has a negative influence on the method as discussed in Section 5.1. Rain was visually observed in the radar images corresponding to the spikes in the time series. The wave model shows a slightly smaller deviation from the ground truth with RMSEs (biases) of 0.16 m (−0.06 m) and 0.12 m (0.03 m), and corresponding NRMSEs of 21%, and 10% at PG_A and PG_B, respectively. Since the wave model was forced at the offshore boundary with the observed wave height at the buoy, it makes no sense to compute an error at this location. Even if the wave model appears to be performing slightly better, the skill of the proposed radar method and the wave model in estimating the significant wave height is comparable. The results show that the proposed radar method can be applied with similar accuracy as numerical wave models, but without the need to know the bathymetry or incident wave height. This is a major benefit in particular for long-term observations.

4.3. Consequences of Simplifications

The bulk approach used in Equation 22 poses the simplest approach to derive the cross-shore distribution of H_s, yet the complicated nonlinear dynamics that occur in a natural breaking wave environment are simplified considerably. Wave directionality, wave reflection, energy losses due to bottom friction, wave growth and shape changes due to wind, nonlinear energy transfers, wave-current interactions, and two-dimensional effects are disregarded. However, parameterizing these effects in a more complete approach would require additional information and include further (unknown) calibration parameters. This is favorable only if it would bring significant improvements in accuracy. In the following, the disregarded aspects are discussed and it is shown that, for the present environment, a simplistic approach is sufficient considering the expected accuracy of the method.

For an oblique wave incidence, the wave celerity and thus the wave and roller energy flux in the cross-shore direction is reduced due to projection effects. The consequences of disregarding this effect were tested through projecting the wave phase and group velocity to the shore normal direction considering the peak direction observed at the buoy and Snell's law to account for refraction along the transect. For the present dataset, the results (in terms of the RMSE) are very similar, with only one cm difference in the RMSE at the buoy, and no difference at the pressure gauges (not shown). This is expectable, because projection factors are above 0.9 (which corresponds to an error in of 5% in terms of H_s) for >87% of the of the grid points between the beach and buoy pressure gauges over the period covered. At the pressure gauges, refraction further decreased the incidence angles and projection factors are above 0.97 for >95% of the data points, thus projection effects can be easily neglected. However, it should also be noted that the wave dissipation is computed from Equation 23, where all other terms are directly estimated from the radar measurements. Since the radar antenna was pointing in the cross-shore direction, the Doppler velocity measurements will also be affected by the same projection angle. It is therefore possible that projection effects are to some extent inherently covered by the proposed method. However, due to the exponential form of the proposed scaling and the complicated dynamics of the water motion in the breaking wave front and their signature in the radar images, it is unclear whether the effects of projection on dU can be explained by simple geometrical considerations. This is something that could be investigated in future experiments.

Frictional losses were estimated as proposed by Thornton and Guza (1983, their eq. 40) by considering the peak period observed at the buoy, the simulated RMS wave height along the transect, and a bed friction coefficient of 0.1. In the growing phase and around the peak of the storm (until Oct 1, 00:00 UTC), the estimated energy flux lost due to bottom friction between the beach and the WR, PG_B, PG_A, were below 8%, 6%, and 2%, of the observed flux at the respective location. The expected relative error in the estimated H_s is below 4%, 3% and 1%, at the WR, PG_B, and PG_A, respectively. Slightly larger (up to 10%) relative errors are estimated for the last couple of hours of the period when only the remaining low-energy swell is present. This is still in the same range as the expected accuracy of the method.

The relative amount of reflected wave energy increases with increasing beach slope and wave period, and decreasing wave energy (Elgar et al., 1994). The maximum slope of the present beach profile (evaluated at scale of the gridded bathymetry, i.e., 5 m, see Section 2) is 0.14 at the beach face (around MSL, see Figure 2). The reflection was estimated as proposed by Ardhuin and Roland (2012, their Equation 13) considering the peak period and root-mean-square wave height observed at the buoy. The estimator of Ardhuin and Roland (2012) is a modified version of the relation used by Elgar et al. (1994) (their Equation 1) which was originally proposed by Miche (1951). The analysis showed that the ratio of reflected and incoming energy is mostly below 1% when wave heights were above 1 m (from Sep 28, 00:00 UTC to Oct 01, 00:00 UTC), slightly larger (1.5%) in the beginning, and up to 8% in the last hours at the end of the period, when wave heights were small (H_s < 0.7 m). Accordingly, the expected error in the estimated H_s when reflection is disregarded is also very small (<1% until Oct 01 00:00 UTC, and <5% afterward). However, since the reflected waves are deshoaling with increasing depth, the estimated errors at the pressure gauges are larger but still below 5% at PG_B, and up to 15%–20% at PG_A.

The effects of disregarding wind growth, white capping, wave-wave and wave-current interactions were not explicitly estimated in the scope of the present study. However, neglecting wind growth and white-capping is a common simplification when surf zone wave transformation is estimated. This is a reasonable assumption because both effects are counteracting and strongly correlated. The residual influence on the variation of wave energy is expected to be more than one order of magnitude smaller than depth induced breaking. Disregarding nonlinear interactions is also reasonable since the wave energy is evaluated over all frequencies in the present

study and the total energy is not affected by energy exchanges within the wave spectrum. The total energy flux will be estimated correctly, if the observed bulk dissipation also includes dissipation at all wave scales, which is something that should be tested in future experiments. Wave induced currents associated with bars and channels and the corresponding circulation may alter the wave celerity and hence the wave energy flux. However, as further explained in Section 5.1, the radar derived dissipation will not be affected by mean currents. The radar derived wave energy flux derived from Equation 24 is therefore also estimated without the influence of currents. However, E_w and H_s derived from the radar are still estimated correctly because currents are also disregarded in Equations 26 and 27.

5. Discussion and Outlook

5.1. Advantages and Limitations

The proposed method provides a radar-based close-range remote sensing technique to reliably observe the transformation of wave energy at a relatively high spatial resolution ($dx = 7.5$ m) over the complete cross-shore transect (>1 km) in energetic wave conditions, thus offering a good balance between accuracy and spatial coverage. Such measurements are complicated to attain using traditional point observation-based wave monitoring systems, for example, arrays of wave buoys, bottom mounted ADCPs or pressure wave gauges. The use of radar expands the spatial coverage of the available close-range remote sensing methods, since lidar, or (IR) video typically have a smaller ground coverage. Radar-based wave height retrieval methods based on the signal-to-noise ratio (e.g., Nieto Borge et al., 2004) or a direct inversion of the Doppler velocity to surface elevation (McGregor et al., 1998) often fail in the nearshore due to the presence of breaking waves. Estimating dissipation from breaking wave signatures instead of wave height is a good alternative, which was used already in other radar-based studies in past (Díaz Méndez et al., 2015; Díaz et al., 2018). However, if the breaking probability is assimilated into a breaking parameterization, as done by Díaz Méndez et al. (2015), it is still needed to estimate the strength of breaking, that is, the amount of energy dissipated by each breaking event. Methods that rely on roller geometry (Díaz et al., 2018) can potentially overcome this, but the limited spatial resolution and complex imaging mechanisms of typically used marine radars prevent a direct estimation of roller geometry, hence a combination of radar and cameras is necessary to obtain geometrical roller properties such as roller length. The method proposed here is self containing and based on roller kinematics, specifically the jump from low to high surface velocities at the toe of a roller, which is represented by the spatial increase of the observed Doppler velocity dU. The Doppler velocity is computed from ensembles of 0.512 s of coherent radar backscatter, which is enough to resolve individual waves with periods longer than ≈3 s. However, the performance of the method at the scale of individual waves remains to be investigated in future studies that involve other data sources that can resolve individual waves (such as lidar). The statistics and dynamics of nearshore breaking waves can be affected by the wind (e.g., Xie, 2017) and by interactions between individual waves such as merging bores (Stringari & Power, 2020) or waves reflected from the shoreline (Martins et al., 2017). This can have an impact on the wave energy dissipation due to breaking. Because the proposed method is technically wave resolving it inherently covers such effects, which are not included in current phase-averaged wave models. Moreover, using the spatial difference dU, rather than the absolute Doppler velocity U_D, brings the major advantage that some influences on the absolute surface velocity, such as the orbital motions of long waves, mean currents or wind induced drift velocities are automatically removed. This is significantly more difficult to implement within video based methods. Furthermore, for many research questions the surface stress is the quantity of interest because it is directly driving wave-induced currents and turbulence production by breakers (e.g., Svendsen, 2005). The primary quantity that is observed by the radar is the roller energy and dissipation, which is closely related to the Reynolds stress acting at the water surface. Estimating roller quantities, as done here, is therefore a more direct measure of the drivers of nearshore circulation compared to wave height measurements. Therefore, it has great potential to be assimilated into numerical models aiming at studying vertically resolved nearshore circulation.

A disadvantage of the proposed method is its inability of dealing with strong rain. Rain induces a strong Doppler signature with a velocity that is correlated with the wind speed (hence the use of weather radar in meteorology). This is problematic for example, in the shadowed regions behind the wave crest, or at the beach where the return signal is low and thus the rain suddenly dominates the backscatter. This can cause large jumps in the observed Doppler velocity which would be misinterpreted as breaking if the increase is positive. Therefore, future developments could involve an automated detection and filtering of rain contaminated regions to avoid this problem.

If the goal is to estimate wave heights, a clear limitation lies in the fact that the energy balance equation must be initialized with the correct wave energy at the model boundary. This could be problematic in locations where substantial reflection is expected, such as steep beaches or rocky coasts, but also when submerged features only partially dissipate the incoming wave energy and the shoreline is not visible in the radar images. However, this issue would not affect the estimates for the roller dissipation. Another requirement for the method is the fact that the jump from slow to fast Doppler speeds at the toe of the breaker must be visible. If the dominant wave length of the wave field is short and the local grazing angle is low, the entire wave trough might be shadowed. In this situation, it would not be possible to estimate the Doppler velocity at the toe of the roller and thus dU is not anymore related to the wave phase speed c. The same behavior is expected if the distance of two successive rollers in the line-of-sight of the radar is smaller than the spatial resolution of the radar. The dissipation rate would then be strongly underestimated. Adjusting β_D to compensate underestimation of c would not help in this case because the error stems from missing information rather than from a systematic bias. For the studied storm event, however, there was no indication for an error of this kind. Assuming monochromatic waves with rollers that are confined in the region between the MWL and the maximum crest elevation η_{crest}, the limiting wave length will depend on η_{crest}, and the grazing angle θ_g and may be roughly estimated from geometrical considerations as $L_{\min} = \eta_{crest}(\tan(\theta_g))^{-1}$. For example, the Doppler signatures of waves with $\eta_{crest} = 1$ m will merge if the wave length is below 4 m, 11 m, and 57 m, for a grazing angles of 1°, 5°, and 15°, respectively. However, a small part of the radar radiation can theoretically also reach geometrically shadowed regions of the wave profile (Plant & Farquharson, 2012). Therefore, the actual lower limits of the method in terms of wave length and local grazing angle remain to be determined experimentally in future studies.

5.2. Generalization and Transferability

The roller concept was originally introduced for spilling breakers in deep water (Duncan, 1981). From laboratory experiments, Duncan (1981) found that the height of the studied quasi-steady breaking waves generated by a towed hydrofoil scales with

$$H = 0.6\,\frac{c^2}{g}. \tag{28}$$

In the present work, Equation 12 was used to substitute the wave height in Equation 9. This scaling is only valid for breaking waves in shallow water. However, the chosen typical values for γ and α_{ad} within Equation 12 yield

$$H = \frac{c^2}{g\left(\frac{1}{0.78} + 0.5\right)} = 0.5612\,\frac{c^2}{g} \approx 0.6\,\frac{c^2}{g}, \tag{29}$$

and thus match the results of Duncan (1981), which suggests that the proposed scaling is also valid for breaking deep water waves. Martins et al. (2018) used a directly measured lower wave height to depth ratio (≈0.5) within Booij's phase speed predictor to relate the phase speed to the wave height. This indicates that the kinematics of bore-like inner surf zone waves differ slightly from the breakers studied by Duncan and the calibration parameter B_r may also need to be adjusted in this regions. Further experiments combining various observational techniques to estimate wave dissipation at different regions of the surf zone are needed to confirm this hypothesis.

Another question that remains open is whether the proposed scaling also provides good results in the transition region between the onset of breaking and the formation of the roller. In this region, the concept of assuming roller dissipation due to the Reynolds stress under the roller does not describe the physics well. It is missing important aspects such as the formation of a plunging jet of water and the corresponding energy transfer when the jet hits the surface. This is expected to be of higher relevance for a plunging breaker type, since for spilling breakers, the roller is formed faster. The roller concept was utilized in the context of the present study to provide a physical basis for the proposed scalings to obtain roller energy (Equation 14) and dissipation (Equation 17) from the Doppler velocity measured by the radar. However, the empirically derived scaling (Equation 20) does not rely on the roller concept. Due to its empirical nature, it must not necessarily be invalid in this region and could potentially also provide good data there. More in-situ data in particular with higher spatial coverage and resolution in the transition region is needed to investigate this hypothesis.

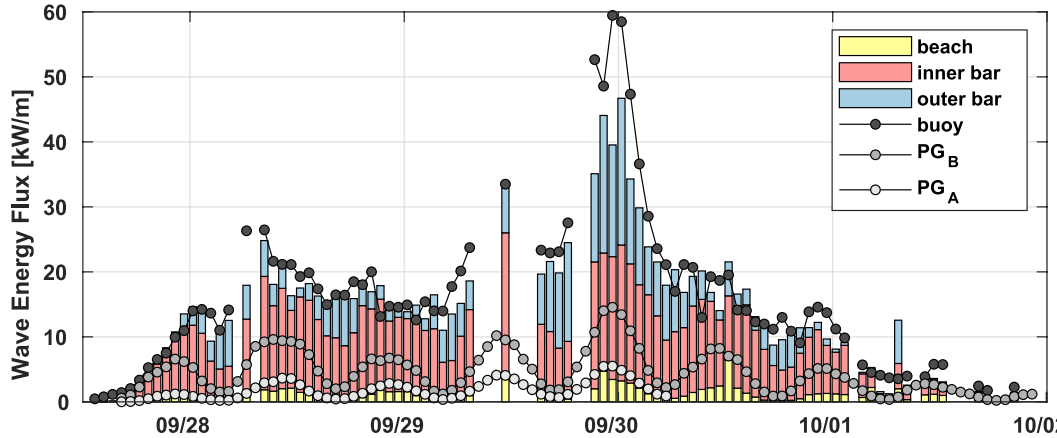

Figure 7. Flux of incoming wave energy measured at the wave rider buoy and the pressure gauges (PG_B and PG_A) together with the radar-derived wave energy flux represented by the bars in the plot. The color coding indicates the energy flux dissipated at the outer bar (between $x = -1{,}100$ m and $x = -330$ m, light blue), the inner bar (between $x = -330$ m and $x = -127.5$ m, light red) and the swash zone at the beach (between $x = -127.5$ m and $x = 0$ m, light yellow).

Future studies may also focus on the extension of the method in the alongshore direction through a utilization of radar data obtained with scanning antenna. However, this is not straight forward because the estimation of the Doppler speeds from scanning radar data is noisier. Therefore the Doppler peak separation algorithm (Streβer et al., 2021) that was used in the present study is not applicable. The sensitivity of the method to an oblique imaging of the incoming waves must also be tested further.

5.3. Exemplary Application: Energy Flux Budget

The radar provides measurements of wave energy flux and dissipation along the complete cross-shore transect every 7.5 m over a distance of more than 1.5 km. This opens the opportunity to quantify and attribute the dissipation of wave energy to different morphological features, the outer bar, the inner bar and the swash zone at the beach. Figure 7 shows the in-situ measurements of the incoming flux of wave energy at the wave rider buoy and the two pressure gauges PG_A and PG_B. The bars in the plot represent the radar-derived flux of wave energy, separated into the portion of energy dissipated at the outer bar, the inner bar, and the swash zone at the beach. At the peak of the storm, when $H_s > 3$ m at the buoy, about 50% of the total incoming wave energy flux is already dissipated at the outer sandbar. This nicely demonstrates the effectiveness of submerged morphological features in reducing the wave energy at the beach during storm conditions. The energy that ends up at the beach shows a dependency on tides, but not so much on the offshore wave height, indicating the expected strong bathymetric control of the nearshore wave heights.

6. Summary and Conclusion

High-resolution (7.5 m) observations of surface wave and roller dissipation are studied along a cross-shore transect of a submesotidal, double-barred, sandy beach in the Southern North Sea. A new close-range remote sensing methodology is introduced to estimate surface roller energy and dissipation from coherent-on-receive marine radar backscatter. Based on the concept of the surface roller, scalings are derived to directly estimate the energy stored within surface rollers, the dissipation of roller energy, and the flux of roller energy from the spatial increase of Doppler velocity observed by the radar at the transition from non-breaking to breaking parts of the sea surface. Ground truthing observations of the dissipation of breaking waves estimated between two bottom mounted pressure wave gauges at an intertidal sandbar were used to empirically assess the proposed method. Optimization of the parameters of an independent empirical power law scaling to the observations yield a similar scaling law as derived from physical principles, which is an indication that the method is reliable even if there are strong assumptions involved in the physical derivation. An assimilation of the observed quantities into the coupled, one-dimensional wave and roller energy flux balance equations also yields the dissipation and flux of organized wave energy along a cross-shore transect over more than one km with a spatial resolution of 7.5 m. For a known

water depth and peak wave period, the significant wave height can be computed from the observed wave energy flux. Comparisons to the in-situ observations at the two pressure gauges and a wave rider buoy, moored about 1 km off the shoreline, indicate a good performance of the proposed method. RMSEs at all locations were below 0.26 m over the course of a storm lasting 3 days, with significant wave heights peaking at 3.3 m. Results from a phase-averaged numerical wave model showed errors below 0.16 m and thus the skill of the radar observation is slightly lower, but comparable to the model. However, no prior knowledge of the bathymetry is required for the radar-based estimates of the wave and roller energy flux and dissipation. This is a major benefit compared to numerical wave models, in particular for locations where rapid bathymetric changes occur, for example, sandy beaches. This new methodology overcomes the difficulties of previously available radar-based wave height retrieval methods, that are not able to provide reliable measurements in the surf zone, mostly due to the influence of wave breaking and increased spatial inhomogeneity. Strong rain and the absence of surface roughness due to low winds are expected to negatively influence the method. However, shore-based radar is relatively easy to install and maintain compared to instruments mounted inside the water. It is able to measure day and night as well as in foggy conditions. This makes the technology perfectly suited for continuous long-term observations with a relatively high spatial and temporal resolution, that are difficult to realize with in-situ instrumentation. The observations are used to investigate wave transformation along a double-barred beach profile and attribute wave energy losses to the morphological features, that is, the outer bar, the inner bar, and the swash zone. Highest roller dissipation rates (>200 W m^{-2}) are found at the inner bar, where also the majority of the incoming wave energy flux is dissipated during moderate conditions. In storm conditions, however, up to 50% of the wave energy is dissipated at the outer bar. This confirms the effectiveness of submerged bathymetric features in reducing wave heights at the beach in energetic wave conditions.

Appendix A: JB07 Wave Breaking Parameterization

The wave breaking parameterization proposed by Janssen and Battjes (2007) (referred to as JB07) approximates the average dissipation of wave energy per unit surface area by depth induced breaking as

$$D_{JB} = \frac{3\sqrt{\pi}}{16} B f_{rep} \rho g \frac{H_{rms}^3}{d} \left[1 + \frac{4}{3\sqrt{\pi}} \left(R^3 + \frac{3}{2}R\right) \exp\left[R^2\right] - \mathrm{erf}(R)\right], \tag{A1}$$

where $R = H_b/H_{rms}$, $H_b = \gamma d$ and B is a calibration factor representing the breaking strength and is set to one. f_{rep} is the representative frequency of the wave field (often the peak frequency is considered). JB07 includes a slight modification of the empirical relationship for the breaker parameter proposed by Battjes and Stive (1985).

$$\gamma = \frac{H_b}{d} = 0.39 + 0.56 \tanh\left(33\, S_0\right), \tag{A2}$$

which depends on the offshore wave steepness $S_0 = (H_{rms}/L)_{\mathrm{offshore}}$. JB07 is similar to an earlier parameterization by Baldock et al. (1998). However, in JB07 the H^3/d dependency is retained instead of substituting it by H^2, as done by Baldock et al. (1998), who assumed that the wave height of a breaker is approximately equal to the water depth, as proposed by Battjes and Janssen (1978). The same modification was coincidentally also reported by Alsina and Baldock (2007) in the same year.

Data Availability Statement

The wave rider buoy data is available from the COSYNA data portal at http://codm.hzg.de/codm. The bathymetry data is available from the PANGAEA data portal at https://doi.org/10.1594/683PANGAEA.898407 (Cysewski et al., 2019). The pressure transducer time series is available at https://doi.org/10.1594/PANGAEA.942014 (Streβer et al., 2022). Post-processed radar observations, wave model results and ground truth used in this study are available from the Zenodo repository at https://doi.org/10.5281/zenodo.5787131(Streßer, 2021). Radar raw data is available from the authors on request.

Acknowledgments
This work was funded by the Helmholtz Association through the program Polar Regions and Coasts in the Changing Earth System (PACES II). The authors would like to thank Dr. Grant Deane, Dr. Jörg Seemann, Marius Cysewski and Ruben Carrasco for fruitful discussions, and two anonymous reviewers for providing constructive comments that have helped to improve the quality of the manuscript significantly. Technical support by Jan Bödewadt and Jurij Stell is highly appreciated. Many thanks to Jens Winkelbauer and Prof. Dr. Peter Fröhle from the Technical University of Hamburg (TUHH) for sharing the design of the pressure loggers. We also acknowledge the support of the "Landesbetrieb für Küstenschutz, Nationalpark und Meeresschutz Schleswig-Holstein" (LKN.SH) in providing the laser scan topography data, and the "Bundesamt für Seeschifffahrt und Hydrographie" (BSH) for extracting the water levels and currents from the operational models.

References

Aarninkhof, S., & Ruessink, B. (2004). Video observations and model predictions of depth-induced wave dissipation. *IEEE Transactions on Geoscience and Remote Sensing*, *42*(11), 2612–2622. https://doi.org/10.1109/TGRS.2004.835349

Alsina, J. M., & Baldock, T. E. (2007). Improved representation of breaking wave energy dissipation in parametric wave transformation models. *Coastal Engineering*, *54*(10), 765–769. https://doi.org/10.1016/j.coastaleng.2007.05.005

Anderson, D., Spicer Bak, A., Brodie, K. L., Cohn, N., Holman, R. A., & Stanley, J. (2021). Quantifying optically derived two-dimensional wave-averaged currents in the surf zone. *Remote Sensing*, *13*(4), 1–20. https://doi.org/10.3390/rs13040690

Ardhuin, F., & Roland, A. (2012). Coastal wave reflection, directional spread, and seismoacoustic noise sources. *Journal of Geophysical Research*, *117*(6), 1. https://doi.org/10.1029/2011JC007832

Baldock, T., Holmes, P., Bunker, S., & Van Weert, P. (1998). Cross-shore hydrodynamics within an unsaturated surf zone. *Coastal Engineering*, *34*(3–4), 173–196. https://doi.org/10.1016/S0378-3839(98)00017-9

Battjes, J. A., & Janssen, J. P. F. M. (1978). *Energy loss and set-up due to breaking of random waves. In Coastal engineering 1978* (Vol. 91, pp. 569–587). American Society of Civil Engineers. https://doi.org/10.1061/9780872621909.034

Battjes, J. A., & Stive, M. J. F. (1985). Calibration and verification of a dissipation model for random breaking waves. *Journal of Geophysical Research*, *90*(C5), 9159. https://doi.org/10.1029/JC090iC05p09159

Bell, P. S., & Osler, J. C. (2011). Mapping bathymetry using X-band marine radar data recorded from a moving vessel. *Ocean Dynamics*, *61*(12), 2141–2156. https://doi.org/10.1007/s10236-011-0478-4

Bergamasco, F., Torsello, A., Sclavo, M., Barbariol, F., & Benetazzo, A. (2017). WASS: An open-source pipeline for 3D stereo reconstruction of ocean waves. *Computers & Geosciences*, *107*(June), 28–36. https://doi.org/10.1016/j.cageo.2017.07.001

Bonneton, P., Lannes, D., Martins, K., & Michallet, H. (2018). A nonlinear weakly dispersive method for recovering the elevation of irrotational surface waves from pressure measurements. *Coastal Engineering*, *138*(June), 1–8. https://doi.org/10.1016/j.coastaleng.2018.04.005

Booij, N. (1981). *Gravity waves on water with non-uniform depth and current. (Unpublished doctoral dissertation)*. TU Delft.

Brown, G. (1998). Guest editorial - special issue on low-grazing-angle backscatter from rough surfaces. *IEEE Transactions on Antennas and Propagation*, *46*(1), 1–2. https://doi.org/10.1109/tap.1998.655445

Carini, R. J., Chickadel, C. C., & Jessup, A. T. (2021a). Surf zone waves at the onset of breaking: 1. LIDAR and IR data fusion methods. *Journal of Geophysical Research: Oceans*, *126*(4), 1–18. https://doi.org/10.1029/2020jc016934

Carini, R. J., Chickadel, C. C., & Jessup, A. T. (2021b). Surf zone waves at the onset of breaking: 2. Predicting breaking and breaker type. *Journal of Geophysical Research: Oceans*, *126*(4), 1–14. https://doi.org/10.1029/2020jc016935

Carini, R. J., Chickadel, C. C., Jessup, A. T., & Thompson, J. (2015). Estimating wave energy dissipation in the surf zone using thermal infrared imagery. *Journal of Geophysical Research: Oceans*, *120*(6), 3937–3957. https://doi.org/10.1002/2014JC010561.Received

Carrasco, R., Horstmann, J., & Seemann, J. (2017). Significant wave height measured by coherent X-band radar. *IEEE Transactions on Geoscience and Remote Sensing*, *55*(9), 5355–5365. https://doi.org/10.1109/TGRS.2017.2706067

Catalán, P. A., Haller, M. C., Holman, R. A., & Plant, W. J. (2011). Optical and microwave detection of wave breaking in the surf zone. *IEEE Transactions on Geoscience and Remote Sensing*, *49*(6 PART 1), 1879–1893. https://doi.org/10.1109/TGRS.2010.2095864

Catalán, P. A., Haller, M. C., & Plant, W. J. (2014). Microwave backscattering from surf zone waves. *Journal of Geophysical Research: Oceans*, *119*(5), 3098–3120. https://doi.org/10.1002/2014JC009880

Chernyshov, P., Vrecica, T., Streßer, M., Carrasco, R., & Toledo, Y. (2020). Rapid wavelet-based bathymetry inversion method for nearshore X-band radars. *Remote Sensing of Environment*, *240*(May 2019), 111688. https://doi.org/10.1016/j.rse.2020.111688

Chickadel, C. C., Holman, R. A., & Freilich, M. H. (2003). An optical technique for the measurement of longshore currents. *Journal of Geophysical Research*, *108*(11), 1–17. https://doi.org/10.1029/2003jc001774

Clark, D. B., Elgar, S., & Raubenheimer, B. (2012). Vorticity generation by short-crested wave breaking. *Geophysical Research Letters*, *39*(24). https://doi.org/10.1029/2012gl054034

Cysewski, M., Streßer, M., Bödewadt, J., Perthun, P., Carrasco, R., & Horstmann, J. (2019). Single beam bathymetry transects at the West coast of Sylt from Sep 22-26 2016 [Dataset]. *PANGAEA*. https://doi.org/10.1594/PANGAEA.898407

Deane, G. B. (1997). Sound generation and air entrainment by breaking waves in the surf zone. *Journal of the Acoustical Society of America*, *102*(5), 2671–2689. https://doi.org/10.1121/1.420321

Deigaard, R., & Fredsøe, J. (1989). Shear stress distribution in dissipative water waves. *Coastal Engineering*, *13*(4), 357–378. https://doi.org/10.1016/0378-3839(89)90042-2

De Vries, S., Hill, D., De Schipper, M., & Stive, M. (2011). Remote sensing of surf zone waves using stereo imaging. *Coastal Engineering*, *58*(3), 239–250. https://doi.org/10.1016/j.coastaleng.2010.10.004

Díaz, H., Catalán, P. A., & Wilson, G. W. (2018). Quantification of two-dimensional wave breaking dissipation in the surf zone from remote sensing data. *Remote Sensing*, *10*(1), 1–17. https://doi.org/10.3390/rs10010038

Díaz Méndez, G. M., Haller, M. C., Raubenheimer, B., Elgar, S., & Honegger, D. A. (2015). Radar remote sensing estimates of waves and wave forcing at a Tidal inlet. *Journal of Atmospheric and Oceanic Technology*, *32*(4), 842–854. https://doi.org/10.1175/JTECH-D-14-00215.1

Dick, S. (2001). *The operational circulation model of BSH (BSHcmod): Model description and validation*. BSH.

Dugan, J. P., Piotrowsky, C. C., Williams, J. Z., Piotrowski, C. C., & Williams, J. Z. (2001). Water depth and surface current retrievals from airborne optical measurements of surface gravity wave dispersion. *Journal of Geophysical Research*, *106*(C8), 16903–16915. https://doi.org/10.1029/2000JC000369

Duncan, J. H. (1981). An experimental investigation of breaking waves produced by a towed hydrofoil. *Proceedings of the Royal Society of London. A. Mathematical and Physical Sciences*, *377*(1770), 331–348. https://doi.org/10.1098/rspa.1981.0127

Elgar, S., Herbers, T. H., & Guza, R. T. (1994). Reflection of ocean surface gravity waves from a natural beach. *Journal of Physical Oceanography*, *24*(7), 1503–1511. https://doi.org/10.1175/1520-0485(1994)024<1503:roosgw>2.0.co;2

Farquharson, G., Frasier, S. J., Raubenheimer, B., & Elgar, S. (2005). Microwave radar cross sections and Doppler velocities measured in the surf zone. *Journal of Geophysical Research*, *110*(12), 1–12. https://doi.org/10.1029/2005JC003022

Feddersen, F., & Trowbridge, J. H. (2005). The effect of wave breaking on surf-zone turbulence and alongshore currents: A modeling study. *Journal of Physical Oceanography*, *35*(11), 2187–2203. https://doi.org/10.1175/JPO2800.1

Flores, R. P., Catalán, P. A., & Haller, M. C. (2016). Estimating surf zone wave transformation and wave setup from remote sensing data. *Coastal Engineering*, *114*(April), 244–252. https://doi.org/10.1016/j.coastaleng.2016.04.008

Goda, Y. (2006). Examination of the influence of several factors on longshore current computation with random waves. *Coastal Engineering*, *53*(2–3), 157–170. https://doi.org/10.1016/j.coastaleng.2005.10.006

Haller, M. C., & Lyzenga, D. R. (2003). Comparison of radar and video observations of shallow water breaking waves. *IEEE Transactions on Geoscience and Remote Sensing*, *41*(4), 832–844. https://doi.org/10.1109/TGRS.2003.810695

Hedges, T. S. (1976). Technical note. An empirical modification to linear wave theory. *Proceedings - Institution of Civil Engineers*, *61*(3), 575–579. https://doi.org/10.1680/iicep.1976.3408

Holman, R., & Haller, M. C. (2013). Remote sensing of the nearshore. *Annual Review of Marine Science*, *5*(1), 95–113. https://doi.org/10.1146/annurev-marine-121211-172408

Holman, R., Plant, N., & Holland, T. (2013). cBathy: A robust algorithm for estimating nearshore bathymetry. *Journal of Geophysical Research: Oceans*, *118*(5), 2595–2609. https://doi.org/10.1002/jgrc.20199

Horstmann, J., Bödewadt, J., Carrasco, R., Cysewski, M., Seemann, J., & Streer, M. (2021). A coherent on receive X-band marine radar for ocean observations. *Sensors*, *21*(23), 7828. https://doi.org/10.3390/s21237828

Janssen, T., & Battjes, J. (2007). A note on wave energy dissipation over steep beaches. *Coastal Engineering*, *54*(9), 711–716. https://doi.org/10.1016/j.coastaleng.2007.05.006

Kimmoun, O., & Branger, H. (2007). A particle image velocimetry investigation on laboratory surf-zone breaking waves over a sloping beach. *Journal of Fluid Mechanics*, *588*, 353–397. https://doi.org/10.1017/S0022112007007641

LKN.SH. (2015). Fachplan Küstenschutz Sylt Historisches zur Entwicklung der Insel Sylt (Einleitung).

Longuet-Higgins, M. S., & Stewart, R. W. (1964). Radiation stresses in water waves; with applications a physical discussion. *Deep-Sea Research*, *11*, 529–562. https://doi.org/10.1016/0011-7471(64)90001-4

Lund, B., Haus, B. K., Horstmann, J., Graber, H. C., Carrasco, R., Laxague, N. J. M., et al. (2018). Near-surface current mapping by shipboard marine X-band radar: A validation. *Journal of Atmospheric and Oceanic Technology*, *35*(5), 1077–1090. https://doi.org/10.1175/jtech-d-17-0154.1

Martins, K., Blenkinsopp, C. E., Almar, R., & Zang, J. (2017). The influence of swash-based reflection on surf zone hydrodynamics: A wave-by-wave approach. *Coastal Engineering*, *122*(December 2016), 27–43. https://doi.org/10.1016/j.coastaleng.2017.01.006

Martins, K., Blenkinsopp, C. E., Deigaard, R., & Power, H. E. (2018). Energy dissipation in the inner surf zone: New insights from Li <scp>DAR</scp> -based roller geometry measurements. *Journal of Geophysical Research: Oceans*, *123*(5), 3386–3407. https://doi.org/10.1029/2017jc013369

Martins, K., Blenkinsopp, C. E., & Zang, J. (2016). Monitoring individual wave characteristics in the inner surf with a 2-dimensional laser scanner (LiDAR). *Journal of Sensors*, *2016*, 1–11. https://doi.org/10.1155/2016/7965431

McGregor, J. A., Poulter, E. M., & Smith, M. J. (1998). S band Doppler radar measurements of bathymetry, wave energy fluxes, and dissipation across an offshore bar. *Journal of Geophysical Research*, *103*(C9), 779–18789. https://doi.org/10.1029/98JC00447

Miche, M. (1951). Le pouvoir réfléchissant des ouvrages maritimes exposés à l'action de la houle. *Annales de Ponts et Chaussées*, *121*, 285–319.

Miret, D., Soriano, G., Nouguier, F., Forget, P., Saillard, M., & Guerin, C. A. (2014). Sea surface microwave scattering at extreme grazing angle: Numerical investigation of the Doppler shift. *IEEE Transactions on Geoscience and Remote Sensing*, *52*(11), 7120–7129. https://doi.org/10.1109/TGRS.2014.2307893

Nairn, R. B., Roelvink, J. A. D., & Southgate, H. N. (1991). Transition zone width and implications for modelling surfzone hydrodynamics. In *Coastal engineering 1990* (Vol. 1, pp. 68–81). American Society of Civil Engineers. https://doi.org/10.1061/9780872627765.007

Navarro, W., Orfila, A., Orejarena-Rondón, A., Velez, J. C., & Lonin, S. (2021). Wave energy dissipation in a shallow coral reef lagoon using marine X-band radar data. *Journal of Geophysical Research: Oceans*, *126*(11), 1–23. https://doi.org/10.1029/2020jc017094

Navarro, W., Velez, J. C., Orfila, A., & Lonin, S. (2019). A shadowing mitigation approach for sea state parameters estimation using X-band remotely sensing radar data in coastal areas. *IEEE Transactions on Geoscience and Remote Sensing*, *57*(9), 6292–6310. https://doi.org/10.1109/TGRS.2019.2905104

Nieto Borge, J., RodrÍguez, G. R., Hessner, K., & González, P. I. (2004). Inversion of marine radar images for surface wave analysis. *Journal of Atmospheric and Oceanic Technology*, *21*(8), 1291–1300. https://doi.org/10.1175/1520-0426(2004)021<1291:iomrif>2.0.co;2

Nieto Borge, J. C., Hessner, K., & Reichert, K. (1999). Estimation of the significant wave height with X-band nautical radars. *Proceedings of the 18th International Conference Offshore Mech (C), 1–8*. Retrieved from http://scholar.google.com/scholar?hl=en{\&}btnG=Search{\&}q=intitle:ESTIMATION+OF+THE+SIGNIFICANT+WAVE+HEIGHT+WITH+X-BAND+NAUTICAL+RADARS{\#}0

O'Dea, A., Brodie, K., & Elgar, S. (2021). Field observations of the evolution of plunging-wave shapes. *Geophysical Research Letters*, *48*(16), 1–10. https://doi.org/10.1029/2021GL093664

Okayasu, A., Shibayama, T., & Mimura, N. (1986). Velocity field under plunging waves. *Coastal Engineering*, *1986*, 660–674. https://doi.org/10.9753/icce.v20.50

Plant, W. J., & Farquharson, G. (2012). Wave shadowing and modulation of microwave backscatter from the ocean. *Journal of Geophysical Research*, *117*(8), 1. https://doi.org/10.1029/2012JC007912

Plant, W. J., Keller, W. C., & Cross, A. (1983). Parametric dependence of ocean wave-radar modulation transfer functions. *Journal of Geophysical Research*, *88*(C14), 9747–9756. https://doi.org/10.1029/JC088iC14p09747

Raubenheimer, B., Elgar, S., & Guza, R. T. (1998). Estimating wave heights from pressure measured in sand bed. *Journal of Waterway, Port, Coastal, and Ocean Engineering*, *124*(3), 151–154. https://doi.org/10.1061/(asce)0733-950x

Rodríguez-Padilla, I., Castelle, B., Marieu, V., Bonneton, P., Mouragues, A., Martins, K., & Morichon, D. (2021). Wave-filtered surf zone circulation under high-energy waves derived from video-based optical systems. *Remote Sensing*, *13*(10), 1874. https://doi.org/10.3390/rs13101874

Rojas, G., & Loewen, M. R. (2010). Void fraction measurements beneath plunging and spilling breaking waves. *Journal of Geophysical Research*, *115*(C8), C08001. https://doi.org/10.1029/2009jc005614

Senet, C. M., Seemann, J., Flampouris, S., & Ziemer, F. (2008). Determination of bathymetric and current maps by the method DiSC based on the analysis of nautical X-band radar image sequences of the sea surface (November 2007). *IEEE Transactions on Geoscience and Remote Sensing*, *46*(8), 2267–2279. https://doi.org/10.1109/TGRS.2008.916474

Senet, C. M., Seemann, J., & Ziemer, F. (2001). The near-surface current velocity determined from image sequences of the sea surface. *IEEE Transactions on Geoscience and Remote Sensing*, *39*(3), 492–505. https://doi.org/10.1109/36.911108

Sinnett, G., & Feddersen, F. (2014). The surf zone heat budget: The effect of wave heating. *Geophysical Research Letters*, *41*(20), 7217–7226. https://doi.org/10.1002/2014GL061398

Streßer, M. (2021). Observed and simulated surface wave and roller dissipation with ground truth data at the West coast of Sylt on Sep 27 - Oct 2, 2016 [Dataset]. *Zenodo*. https://doi.org/10.5281/zenodo.5787131

Streßer, M., & Horstmann, J. (2019). Remote quantification of nearshore wave energy dissipation rates from coherent X-band radar backscatter. *2019 IEEE/OES Twelfth Current, Waves and Turbulence Measurement (CWTM)*, 1–6. https://doi.org/10.1109/CWTM43797.2019.8955284

Streßer, M., Horstmann, J., Winkelbauer, J., & Stell, J. (2022). Absolute pressure at the sea floor at the West coast of Sylt from Sept 27 to Oct 6, 2016 [Dataset]. *PANGAEA*. https://doi.org/10.1594/PANGAEA.942014

Streßer, M., Seemann, J., Carrasco, R., Cysewski, M., Horstmann, J., Baschek, B., & Deane, G. (2021). On the interpretation of coherent marine radar backscatter from Surf Zone waves. *IEEE Transactions on Geoscience and Remote Sensing*. https://doi.org/10.1109/TGRS.2021.3103417

Stringari, C. E., & Power, H. E. (2020). Quantifying bore-bore capture on natural beaches. *Journal of Geophysical Research: Oceans*, *125*(6), 1–16. https://doi.org/10.1029/2019jc015689

Svendsen, I. A. (1984). Wave heights and set-up in a surf zone. *Coastal Engineering*, *8*(4), 303–329. https://doi.org/10.1016/0378-3839(84)90028-0

Svendsen, I. A. (2005). Introduction to nearshore hydrodynamics. *World Scientific*, *24*. https://doi.org/10.1142/5740

Thornton, E. B., & Guza, R. T. (1983). Transformation of wave height distribution. *Journal of Geophysical Research*, *88*(C10), 5925. https://doi.org/10.1029/jc088ic10p05925

Van Eijk, A. M., Kusmierczyk-Michulec, J. T., Francius, M. J., Tedeschi, G., Piazzola, J., Merritt, D. L., & Fontana, J. D. (2011). Sea-spray aerosol particles generated in the surf zone. *Journal of Geophysical Research*, *116*(19), 1–20. https://doi.org/10.1029/2011JD015602

Voulgaris, G., & Collins, M. B. (2000). Sediment resuspension on beaches: Response to breaking waves. *Marine Geology*, *167*(1–2), 167–187. https://doi.org/10.1016/S0025-3227(00)00025-6

Xie, Z. (2017). Numerical modelling of wind effects on breaking waves in the surf zone. *Ocean Dynamics*, *67*(10), 1251–1261. https://doi.org/10.1007/s10236-017-1086-8